RSC Advances

ROYAL SOCIETY OF CHEMISTRY

www.rsc.org/advances

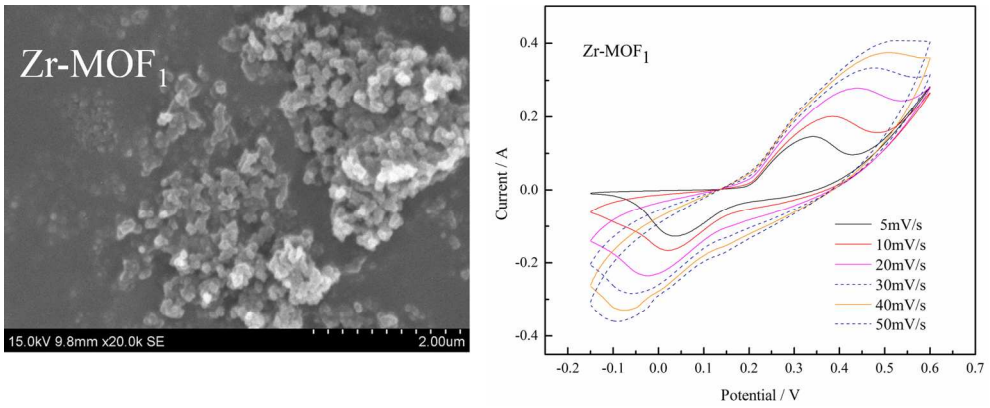

A facile synthetic method was developed to prepare Zr-MOFs.
Pseudo capacitor behavior in KOH electrolyte.
Zr-MOF1 with small particle size exhibited higher supercapacitive performance.
159x65mm (300 x 300 DPI)

Facile synthesis and supercapacitive properties of Zr-metal organic frameworks (UiO-66)

Yueyue Tan, Wei Zhang, Yilong Gao, Jianxiang Wu, Bohejin Tang*

College of Chemistry and Chemical Engineering, Shanghai University of Engineering Science,

Shanghai 201620, China

*Corresponding author: Tel: +86-021-67791214 Fax: +86-021-67791214

*E-mail address: tangbohejin@sues.edu.cn

Abstract: Metal organic frameworks (MOFs) as a kind of crystalline porous materials have attracted much attention due to their high surface area and controllable porous structure. In this paper, we present a new synthesis of Zr-based MOFs with high electrochemical performance by a facile synthetic method of changing the reaction temperature and stirring condition. By varying the reaction temperatures, the different particle sizes and the degree of crystallization can be modified. This paper is focused on the electrochemical properties of Zr-based MOFs as electrode materials in supercapacitors. A maximum specific capacitance of Zr-MOF_1 obtained at 50 °C can reach up to 1144 F g^{-1} at a scan rate of 5 mV s^{-1}, which is far higher than Zr-MOF_2 (811 F g^{-1}), Zr-MOF_3 (517 F g^{-1}) and Zr-MOF_4(207 F g^{-1}), respectively. The results of electrochemical measurements show that the Zr-MOF_1 we synthesized has excellent capacitance performance and good cycling stability over 2000 cycles, which makes it a promising supercapacitor electrode material.

Keyword: Metal organic frameworks, supercapacitor, porous materials, UiO-66

1. Introduction

In response to the ever increasing demand of energy storage devices with high power density, supercapacitors have been widely investigated as next-generation power storage devices to replace

lithium ion batteries due to their longer cycle life, faster charging-discharging speed and lower maintenance cost.[1-4]

Metal-organic frameworks (MOFs) as a new class of porous crystalline materials have been employed in a variety of prospective applications including catalysis[5-7], gas capture-storage[8, 9]/separation[10] and selective adsorption.[11-13] UiO-66 is a 3D MOF composed of a zirconia-based inorganic building brick and terephthalate (BDC) as organic linker, whose structure is built up from the $Zr_6O_4(OH)_4$ oxoclusters bounded to twelve terephthalate (BDC) ligands (Figure 1).[5, 14] UiO-66 features an arrangement of secondary building units (SBUs) which is topologically equivalent to a cubic close-packing.[15] The UiO-66 family possesses a good thermal stability (up to 773 K),[16] and an outstanding chemical stability with regard to water, ethanol, benzene and *N*,*N*-dimethylformamide (DMF).[17] The exceptional stability of UiO-66 can be attributed to strong Zr–O bonds within the characteristic SBU and to the high degree of interlinking of these SBUs, which has attracted many scientists' attention in recent years, resulting in a significant increase in the work based on the Zr-MOF system.

The synthesis and modification of Zr-based frameworks (UiO-66) are discussed along with their unique properties and potential technological utility. Generally, UiO-66 was synthesized from a mixture containing equimolar amounts of $ZrCl_4$, terephthalic acid (BDC), and HCl in DMF, with addition of benzoic acid or acetic acid as a modulator to facilitate crystallization.[18] In case of the synthesis of UiO-66, Gesa Wißmann et al. were able to vary the size of individual nanocrystals using a modulation approach.[15] In our present work, UiO-66 with different particle sizes was obtained by a facile synthetic method of changing the reaction temperature and stirring condition, which is controllable and feasible. As far as our knowledge goes, there have only been few systematic studies on the application of

UiO-66 in supercapacitors.[19-21] However, these materials have low specific capacitance such as the Co-MOF reported by D. Y. Lee et al. just up to 207.76 F g^{-1}.[19] Herein, we present such a study on a Zr-based MOF with higher electrochemical performance.

2. Experimental

2.1 Synthesis of four kinds of Zr-MOFs

All the chemicals were obtained from Aladdin and used without further purification. The synthetic procedure of four kinds of Zr-MOFs was performed by dissolving $ZrCl_4$ (0.227 mmol, 98%) and BDC (0.227 mmol, 98.9%) in 26 g DMF (99%) in a 100 mL round bottomed flask and adding HCl (0.52 g) to the slurry dropwise under stirring conditions. Solvothermal treatment of the slurry was at the corresponding temperatures of 50, 70, 90 and 110 °C under continuous magnetic stirring for 24 h. Subsequently, the resulting white precipitate was centrifuged, washed with 10 mL DMF for five times and dried under vacuum at 120 °C for 16 h. The as-prepared samples were denoted to Zr-MOF_1, Zr-MOF_2, Zr-MOF_3, Zr-MOF_4, respectively.

2.2. Structural characterization

X-ray powder diffraction patterns were obtained with an X-ray diffraction meter (D/Max-rB) using Cu Kα radiation (λ=1.54056 Å), with accelerating voltage and current of 50 kV and 100 mA, respectively. Scanning electron micrographs (SEM) analysis (HITACHI S-3400N) was used to capture and further determine the morphologies and the particle size of the crystalline Zr-MOFs. N_2 adsorption–desorption isotherms of the as-prepared samples were measured at the temperature of liquid N_2 (77 K) using a Micromeritics ASAP 2460 analyzer. The specific surface area was calculated with the Brunauer-Emmett-Teller (BET) equation.

2.3. Electrode preparation and electrochemical performance test

The electrode was prepared according to the following steps: The mixture containing 75 wt% composite materials, 20 wt% electrical conductors (super P) and 5 wt% polytetrafluoroethylene (PTFE, 60 wt% dispersion in H_2O) binder was well mixed in ethanol and then pressed onto nickel foam that serves as a current collector. The prepared electrode was dried at 90 ºC oven for 2 h. The electrode of Zr-MOF_1, Zr-MOF_2, Zr-MOF_3 and Zr-MOF_4 contained about 5.775, 5.400, 5.775 and 5.475 mg electroactive materials, respectively.

All electrochemical measurements were performed on a CHI600D electrochemical workstation in 6 M KOH aqueous electrolyte in a three-electrode system, consisting of the active material electrode as working electrode, a saturated calomel electrode (SCE) as reference electrode and a platinum sheet electrode as counter electrode, respectively.

3. Results and discussion

3.1. Structure of the Zr-MOFs

The X-ray diffraction patterns given in Fig. 2 reveal that the structure of the Zr-MOFs obtained at different temperatures. The UiO-66 structure was solved from the powder XRD pattern, and it can be seen that all the positions of diffraction peaks of as-synthesized Zr-MOF are the same as the profile of UiO-66 synthesized previously by Cavka et al..[22] From the XRD patterns in Fig. 1, one can see that the peak intensity from Zr-MOF_1 to Zr-MOF_4 gradually increased with the increase of reaction temperature, which also clearly indicates Zr-MOF_4 has better crystallinity compared to Zr-MOF_1, Zr-MOF_2 and Zr-MOF_3.

Figure.3 displays SEM images of as-synthesized Zr-MOFs obtained by solvothermal reaction for 24 h. SEM images reveal further changes due to the influence of temperature, which demonstrate that

homogeneous particles of Zr-MOFs were obtained and the particle sizes for Zr-MOF_1, Zr-MOF_2, Zr-MOF_3 and Zr-MOF_4 are around 100, 200, 450 and 500 nm , respectively. In the previous report by Cavka et al.,[22] the particle size of Zr-MOF was 200 nm[16]. This suggests that smaller size particles could be obtained via changing the reaction temperature and stirring condition.

The Nitrogen adsorption–desorption isotherms of four kinds of Zr-MOFs are shown in Fig. 4. The samples were degassed in N_2 at 200°C for 16 h prior to the measurements. It is worth noting that the BET specific surface area of Zr-MOF_1 is 1047 $m^2 g^{-1}$, which is much higher than that of Zr-MOF_2 (933 $m^2 g^{-1}$), Zr-MOF_3 (732 $m^2 g^{-1}$), and Zr-MOF_4 (596 $m^2 g^{-1}$).

3.2. Electrochemical performances of the Zr-MOFs as electrode materials for supercapacitor

The electrochemical behaviors of Zr-MOF_1, Zr-MOF_2, Zr-MOF_3 and Zr-MOF_4 electrodes were measured using cyclic voltammetry at various scan rates (from 5 to 50 mV s^{-1}), as shown in Fig. 5. In an electrochemical capacitor, the charge is accumulated in the double layers mainly by electrostatic force. However, in our work, quasi-symmetric redox peaks are visible in the CV curves, indicating that the measured capacitance is mainly based on a redox mechanism—different from that of electric double layer capacitors with a CV curve close to an ideal rectangular shape. In other words, one can claim that the ions are adsorbed on the electrode surface by the reversible electrochemical reactions. The result demonstrated that the four kinds of Zr-MOFs exhibit inferior electrochemical capacitance performance with increasing the reaction temperature from 50 to 110 °C. The single Zr-MOF_1 electrode showed a specific capacitance (SC) as high as 1144 F g^{-1} at scan rate of 5 mV s^{-1} in 6 M KOH in a three-electrode configuration, which can be ascribed to the redox reactions taking place in the surface of the electrode. Furthermore, the smaller particles for the Zr-MOFs we synthesized are reckoned to facilitate fast redox reactions and short diffusion paths for electrons and ions. The 3D structure of the

Zr-MOFs not only reduces the diffusion resistance of electrolytes but also enhances the facility of ion transportation and maintains the very smooth electron pathways in the very rapid charge/discharge reactions. In addition, the larger surface area for Zr-MOF_1 (1047 m^2 g^{-1}) electrode is utilized efficiently to accommodate large number of charges which enables to achieve capacitances higher than those in Zr-MOF_2, Zr-MOF_3, Zr-MOF_4. Such high specific capacitance is much higher than that of many MOFs, such as the ZIF-8 (~99 F g^{-1}) electrodes,[23] the Co-MOF (206.76 F g^{-1})[19] and so on, indicating it may become a very promising electrode for high-energy and high-power supercapacitors. For Zr-MOF_2, Zr-MOF_3 and Zr-MOF_4 electrodes, the SC values are 811, 517 and 207 F g^{-1} at a scan rate of 5 mV s^{-1}, respectively. Note that with the scan rate increased, the shape of the CV changed, the anodic peak potential and cathodic peak potential shift in more anodic and cathodic directions, respectively, and the capacitance, inevitably, decreased, which is consistent with the following result of galvanostatic charge-discharge measurement.

The specific capacitances at different scan rates are shown in Fig. 6a for all Zr-MOFs samples. The specific capacitance at a given scan rate v can be estimated from voltammetric response by the following equation[24]: $C = \frac{1}{vm}\int \frac{I}{V} dV$ where C is the specific capacitance (F/g), v is the scan rate (V/s), m is the mass of the active material (g), I and V are the current density (A) and the corresponding voltage(V),respectively. A maximum SC value of 1144 F g^{-1} was obtained at a CV scan rate of 5 mV s^{-1} and an SC value of 369 F g^{-1} was obtained even at a scan rate of 50 mV s^{-1}, indicating the material exhibits high power density. However, it is clear from Fig. 5a that the decrease in specific capacitance for four kinds of Zr-MOFs is apparent with the increase of scan rate.

In order to further evaluate the electrochemical performance of four kinds of Zr-MOFs in 6M KOH aqueous solution, the galvanostatic charge-discharge curves were measured at a current density of 5

$mA \cdot cm^{-2}$, as shown in Fig. 6b. No obvious voltage drop can be observed at the beginning of the discharge process for all the Zr-MOFs samples. The shape of the discharge curves suggests the pseudo-capacitive nature of the material, which is consistent with the result of the CV curves. The nonlinear potential variation of charging/discharging profiles signifies the pseudocapacitance behavior of electrodes, which results from the redox reaction or electrochemical adsorption/desorption at the interface at certain potentials.

The electrochemical impedance spectroscopy (EIS) technique was employed to further analyze the electrochemical frequency behavior of all the samples in 6 M KOH solution, as shown in Fig. 6c. A single semicircle in the high frequency region is attributed to the internal resistance and capacitance. A linear inclination in the low frequency region is due to the diffusion of electrolyte ions appeared during charging-discharging process. The internal resistances (R_s) of the Zr-MOF_1, Zr-MOF_2 and Zr-MOF_3 and Zr-MOF_4 electrodes are 0.42, 0.53, 0.60 and 0.62 Ω, respectively, manifesting the Zr-MOF_1 electrode obtained at 50 °C shows a lower internal resistance.

For a useful pseudocapacitor, the long-term cycle stability of electrode materials is another critical requirement, so an endurance test (Fig.6d) of the Zr-MOF_1 electrode was conducted using 2000 CV cycles between -0.05 and 0.7 V at the scan rate of 10 mV s^{-1}. It can be seen that the specific capacitance of the Zr-MOF_1 electrode remains 654 F g^{-1} over 2000 cycles, indicating a relatively good stability of the material. These results revealed the high specific capacitance and remarkable rate capability of Zr-MOF_1 for high-performance electrochemical pseudocapacitors.

4. Conclusions

In summary, four kinds of high-performance Zr-MOFs were successfully synthesized by changing the reaction temperature (from 50 to 110 °C) and under stirring condition. The specific capacitance of the

Zr-MOF_1 electrode is as high as 1144 F g^{-1} at scan rate of 5 mV s^{-1}. From the electrochemical tests, we can conclude that the Zr-MOFs showed an excellent electrochemical performance and have potential application in electrode material for pseudocapacitors.

Acknowledgments

This work was supported by the Fund of Graduate Innovation Project, College of Chemistry and Chemical Engineering, Shanghai University of Engineering Science (E-0903-14-01106).

Reference

1. O. Erdinc, B. Vural and M. Uzunoglu, *Journal of Power sources*, 2009, 194, 369-380.
2. Y. Cai, Y. Wang, S. Deng, G. Chen, Q. Li, B. Han, R. Han and Y. Wang, *Ceramics International*, 2014, 40, 4109-4116.
3. Y. J. Oh, J. J. Yoo, Y. I. Kim, J. K. Yoon, H. N. Yoon, J.-H. Kim and S. B. Park, *Electrochimica Acta*, 2014, 116, 118-128.
4. P. Simon and Y. Gogotsi, *Nature materials*, 2008, 7, 845-854.
5. A. Corma, H. Garcia and F. Llabrés i Xamena, *Chemical Reviews*, 2010, 110, 4606-4655.
6. F. X. Llabrés i Xamena, A. Abad, A. Corma and H. Garcia, *Journal of Catalysis*, 2007, 250, 294-298.
7. J. Lee, O. K. Farha, J. Roberts, K. A. Scheidt, S. T. Nguyen and J. T. Hupp, *Chemical Society Reviews*, 2009, 38, 1450-1459.
8. K. Sumida, D. L. Rogow, J. A. Mason, T. M. McDonald, E. D. Bloch, Z. R. Herm, T.-H. Bae and J. R. Long, *Chemical reviews*, 2011, 112, 724-781.
9. M. P. Suh, H. J. Park, T. K. Prasad and D.-W. Lim, *Chemical reviews*, 2011, 112, 782-835.
10. J.-R. Li, J. Sculley and H.-C. Zhou, *Chemical reviews*, 2011, 112, 869-932.
11. P. L. Llewellyn, S. Bourrelly, C. Serre, A. Vimont, M. Daturi, L. Hamon, G. De Weireld, J.-S. Chang, D.-Y. Hong and Y. Kyu Hwang, *Langmuir*, 2008, 24, 7245-7250.
12. K. Sumida, M. R. Hill, S. Horike, A. Dailly and J. R. Long, *Journal of the American Chemical Society*, 2009, 131, 15120-15121.
13. M. E. Davis, *Nature*, 2002, 417, 813-821.
14. Q. Yang, A. D. Wiersum, H. Jobic, V. Guillerm, C. Serre, P. L. Llewellyn and G. Maurin, *The Journal of Physical Chemistry C*, 2011, 115, 13768-13774.
15. G. Wißmann, A. Schaate, S. Lilienthal, I. Bremer, A. M. Schneider and P. Behrens, *Microporous and Mesoporous Materials*, 2012, 152, 64-70.
16. H. R. Abid, H. Tian, H.-M. Ang, M. O. Tade, C. E. Buckley and S. Wang, *Chemical Engineering Journal*, 2012, 187, 415-420.
17. P. S. Bárcia, D. Guimarães, P. A. Mendes, J. A. Silva, V. Guillerm, H. Chevreau, C. Serre and A. E. Rodrigues, *Microporous and Mesoporous Materials*, 2011, 139, 67-73.
18. F. Vermoortele, B. Bueken, G. Le Bars, B. Van de Voorde, M. Vandichel, K. Houthoofd, A.

Vimont, M. Daturi, M. Waroquier and V. Van Speybroeck, *Journal of the American Chemical Society*, 2013, 135, 11465-11468.

19. D. Y. Lee, S. J. Yoon, N. K. Shrestha, S.-H. Lee, H. Ahn and S.-H. Han, *Microporous and Mesoporous Materials*, 2012, 153, 163-165.
20. D. Y. Lee, D. V. Shinde, E.-K. Kim, W. Lee, I.-W. Oh, N. K. Shrestha, J. K. Lee and S.-H. Han, *Microporous and Mesoporous Materials*, 2013, 171, 53-57.
21. R. Díaz, M. G. Orcajo, J. A. Botas, G. Calleja and J. Palma, *Materials Letters*, 2012, 68, 126-128.
22. J. H. Cavka, S. Jakobsen, U. Olsbye, N. Guillou, C. Lamberti, S. Bordiga and K. P. Lillerud, *Journal of the American Chemical Society*, 2008, 130, 13850-13851.
23. Y. Gao, J. Wu, W. Zhang, Y. Tan, J. Zhao and B. Tang, *Materials Letters*, 2014, 128, 208-211.
24. N. A. M. Barakat, A. G. El-Deen, G. Shin, M. Park and H. Y. Kim, *Materials Letters*, 2013, 99, 168-171.

Figures capations

Fig. 1. Illustration of the UiO-66(Zr) crystalline structure (Zr polyhedra, blue; C, gray; O, red). Hydrogen atoms on the organic linkers were omitted for clarity. The large yellow spheres represent the void regions inside the cages.

Fig. 2. XRD patterns of the Zr-MOFs including Zr-MOF_1, Zr-MOF_2, Zr-MOF_3, Zr-MOF_4, respectively.

Fig. 3. SEM images of as-synthesized Zr-MOFs obtained at different temperatures.

Fig. 4. CV curves of different samples at various scanning rates. (a) Zr-MOF_1; (b) Zr-MOF_2; (c) Zr-MOF_3; (d) Zr-MOF_4;

Fig.5. Nitrogen adsorption–desorption isotherm of Zr-MOF_1, Zr-MOF_2,(c) Zr-MOF_3, (d) Zr-MOF_4.

Fig.6. (a) The specific capacitance as a function of scan rate of different samples; (b) Galvanostatic charge/discharge curves of different samples at a current density of 5 $mA \cdot cm^{-2}$.; (c) EIS of different samples; (d) Cycling performance of Zr-MOF_1 at scan rate of 10 mV s^{-1}.

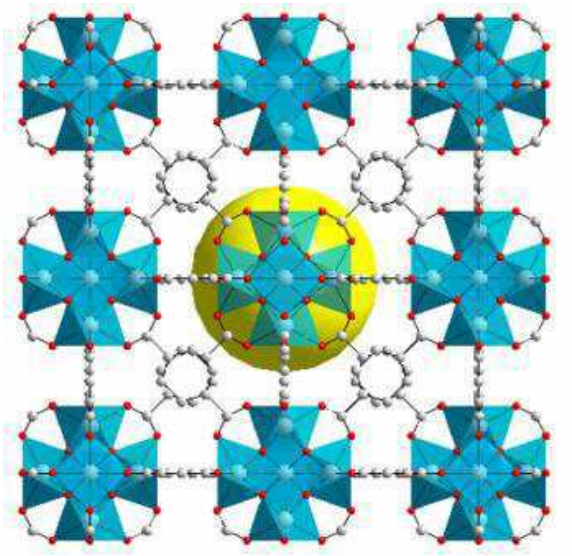

Fig. 1

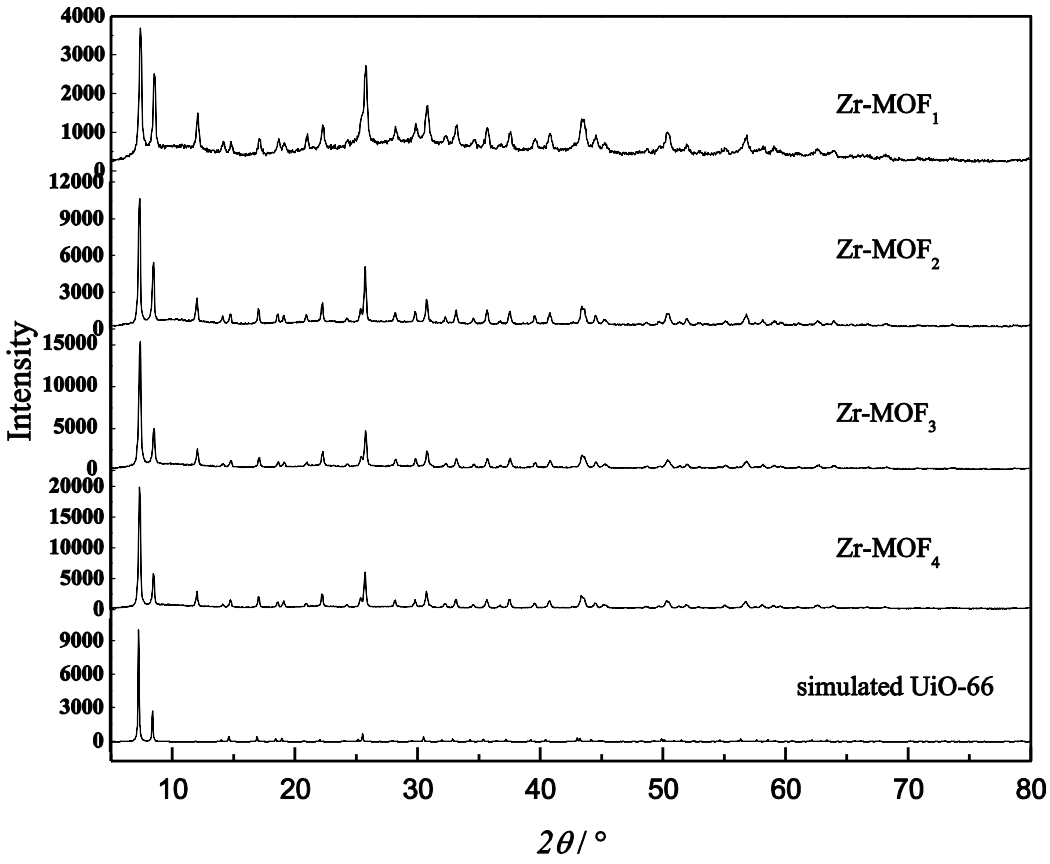

Fig. 2

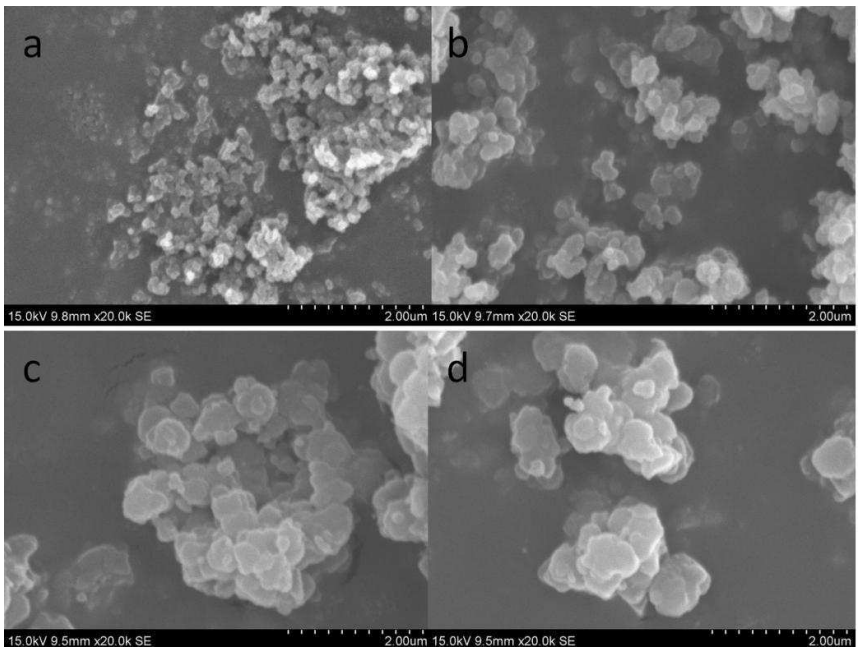

Fig. 3

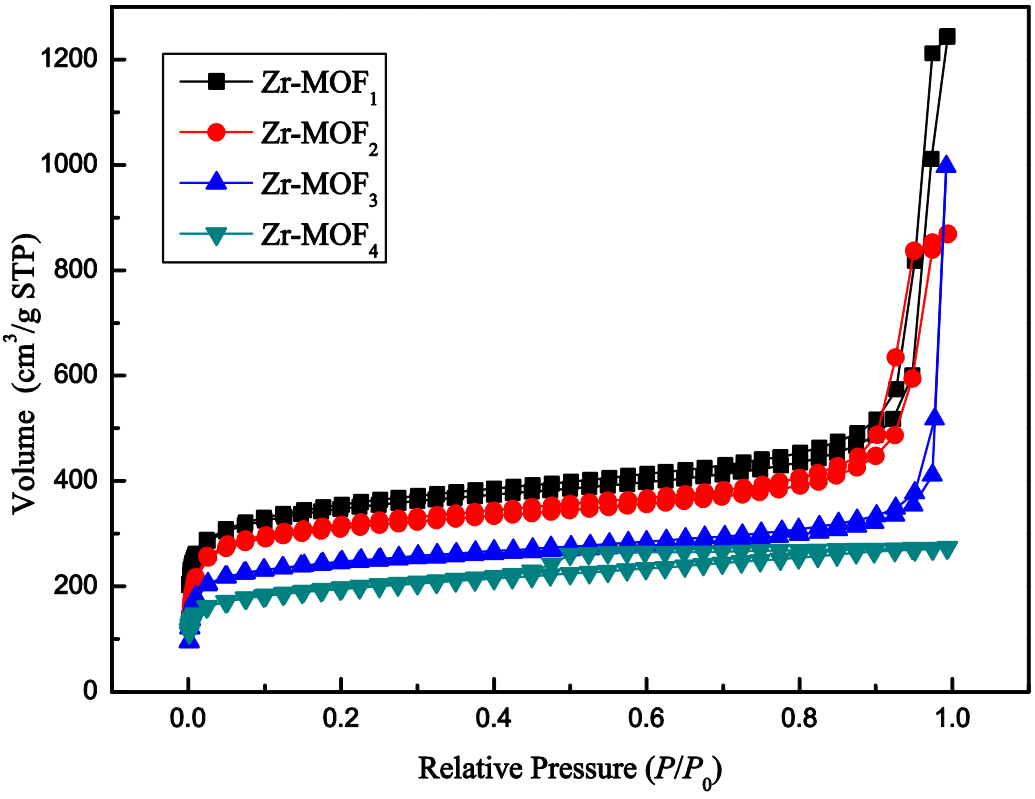

Fig. 4

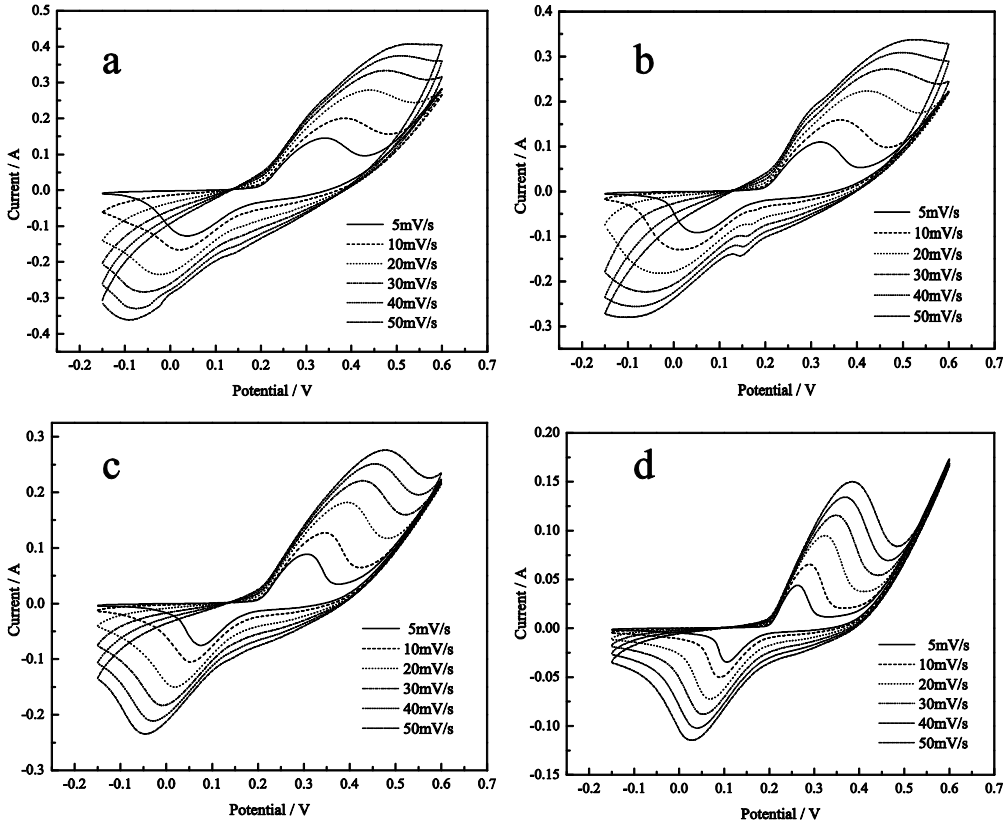

Fig. 5

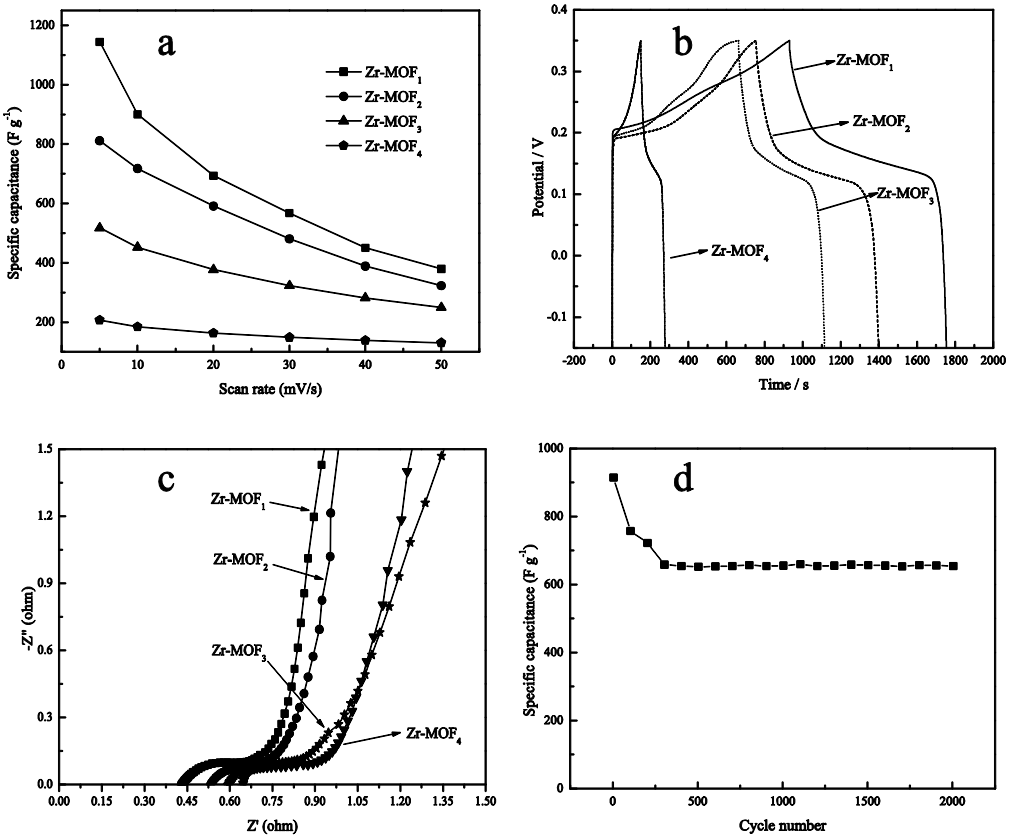

Fig. 6